Sensors and Materials, Vol. 38, No. 3 (2026) 1417–1427
MYU Tokyo

S & M 4385

Manufacturing and Characterization of Complementary Metal Oxide Semiconductor-based Thermoelectric Infrared Sensors with a Ring-shaped Aluminum Grating Absorber

Zhi-Xuan Dai* and Yu-Nuo Liu

Department of Bio-Industrial Mechatronics Engineering, National Chung Hsing University,
No. 145 Xingda Rd., South Dist., Taichung City 402202, Taiwan (R.O.C.)

(Received July 15, 2025; accepted December 24, 2025)

Keywords: infrared sensor, thermoelectric, thermopile, microelectromechanical systems, complementary metal oxide semiconductor process

We present the design, fabrication, and characterization of a thermoelectric IR sensor based on the standard 0.35 μm CMOS process. The sensor features 32 thermopile junctions with centrally located hot ends and a ring-shaped aluminum grating absorber, both configured as suspended structures to enhance thermal isolation and improve temperature sensitivity. The cold ends of the thermopiles are anchored to the silicon substrate to establish a temperature gradient under IR exposure. The device was fabricated through Taiwan Semiconductor Manufacturing Company (TSMC) processes. A two-step post-CMOS etching process—using CF_4/O_2 and SF_6/O_2 reactive ion etching—was employed to create cavities beneath the suspended regions, minimizing thermal losses and enhancing output performance. The sensor's voltage responsivity reached 276 V/W. Additionally, dynamic response testing using a modulated IR source and an optical chopper revealed a response time of 2.2 ms. The proposed sensor demonstrates high sensitivity, fast response, and compatibility with large-scale semiconductor manufacturing.

1. Introduction

IR sensors have a wide range of applications across industrial, medical, and consumer domains. One of the most common uses is in human detection and motion sensing, where passive infrared sensors detect body heat to trigger lighting, alarms, or automation systems.(1) In thermal imaging and night vision, IR cameras capture heat patterns and are essential for low-light object detection in surveillance and autonomous vehicles.(2) In environmental and safety monitoring, nondispersive IR sensors are used for precise gas detection—notably CO_2—in heating, ventilation, and air conditioning (HVAC) systems and air quality monitors.(3) In noncontact temperature sensing, IR thermometers enable the measurement of object temperature from a distance, which became crucial during the COVID-19 pandemic.(4) Flame detection is another critical industrial application where IR sensors are used to identify flame signatures in gas turbines or chemical plants to prevent hazards.(5) In the biomedical field, IR-based

*Corresponding author: e-mail: zxdai@nchu.edu.tw
https://doi.org/10.18494/SAM5944

ISSN 0914-4935

photoplethysmography (PPG) sensors are integrated into smartwatches to monitor heart rate and blood oxygen by measuring blood volume changes.[6] In agriculture, thermal IR sensors help monitor plant water stress and canopy temperature, enabling smarter irrigation.[7] Within manufacturing, IR sensors are applied in process control for real-time temperature feedback during plastic molding or welding operations.[8] For gesture recognition and proximity sensing, NIR sensors detect hand gestures and face proximity in smartphones and human–machine interface systems.[9] Lastly, in structural health monitoring, infrared thermography is a nondestructive technique used to identify defects such as delamination or cracks in concrete structures and bridges.[10] These versatile applications underscore the vital role of IR sensors in modern technology.

MEMS technology enables the integration of components,[11–16] sensors,[17–22] actuators,[23–26] and electronics on a single silicon substrate using microfabrication processes. Its major advantages include miniaturization, low power consumption, and mass production capability. When applied to IR sensors, MEMS allows the development of highly sensitive, compact thermopile detectors with fast thermal response and low-cost batch manufacturing.[27,28] These MEMS-based IR sensors operate at room temperature without requiring cooling or bias voltage, making them ideal for applications such as noncontact temperature measurement, environmental monitoring, and gas detection.[29,30] MEMS-based infrared sensors with various material and structural innovations have recently been explored. For instance, Bao *et al.*[31] developed a MEMS thermopile IR sensor utilizing dual-layer thermocouples made from P-polysilicon and N-polysilicon, separated by a silicon dioxide insulation layer. Patterned aluminum wires connected the thermocouples to enable efficient Seebeck-effect-based voltage generation. The device used a silicon nitride absorber and complementary CMOS-compatible processes with etch-stop layers to minimize release damage during isotropic XeF_2 etching. While this approach improves responsivity and enables miniaturization, it introduces high device resistance and complex alignment challenges during fabrication. Lee *et al.*[32] introduced a MEMS pyroelectric IR sensor using a ZnO thin film as the sensing layer, with Cr/Au electrodes. Built on a thermally insulated silicon substrate with variable thickness, the sensor was fabricated using low-pressure CVD (LPCVD), RF sputtering, photolithography, and etching. A partially covered mesh electrode design enhanced thermal response and charge collection. Although it achieved high responsivity, limitations include structural fragility and a reduced sensing range at longer distances. Similarly, Tsai *et al.*[33] employed a ZnO thin film in their MEMS pyroelectric IR sensor, integrated between Cr/Au electrodes on a thermally isolated Si substrate with Si_3N_4 insulation. Fabricated by LPCVD, RF magnetron sputtering, and KOH wet etching, the device was annealed at 500 °C to enhance ZnO crystallinity and responsivity. Despite promising voltage responses and system integration, drawbacks included short detection ranges and high-precision process requirements that impact cost and scalability. Padha *et al.*[34] focused on wearable MEMS/nano-EMS (NEMS)-based IR sensors for healthcare applications. These devices often include thermopiles or microbolometers made from VO_x or amorphous silicon on flexible substrates. Fabrication involves thin-film deposition, lithography, and micromachining. Although these designs provide high sensitivity and miniaturization, challenges include thermal cross-talk, environmental sensitivity, and complex integration with flexible electronics, which

affect reliability. Ho *et al.*[35] developed a MEMS pyroelectric IR sensor featuring a $PbTiO_3$ film on a silicon cantilever. The multilayer design includes a gold black absorber, a $PbTiO_3$ film, and an aluminum electrode. Micromachining and RF sputtering were used for fabrication. While offering improved current responsivity and faster response, the sensor's thin substrate leads to mechanical fragility and performance degradation under excessive heat conduction. Ahmadzadeh *et al.*[36] fabricated an enhanced thermopile sensor with a two-layer carbon absorber: a nonhydrogenated layer for strong IR absorption and a hydrogenated overcoat to reduce reflectance. Built on a CMOS-compatible MEMS platform through pulsed DC sputtering at room temperature, the design significantly improves output voltage. However, challenges include film stress and decreased absorptance when hydrogen content is high. Adiyan *et al.*[37] proposed a biomaterial cantilever IR sensor made of 150-nm-thick aluminum and silicon nitride layers that bend under IR exposure owing to different thermal expansion rates. The sensor uses a 20-μm-thick biomaterial and 40-μm-long isolation legs, fabricated with a standard MEMS process. A prism-based optical readout with transverse magnetic polarized light enhances sensitivity. Limitations include fabrication complexity, array nonuniformity, and mechanical alignment sensitivity. Lei *et al.*[38] presented thermopile IR sensors on suspended films using P-polysilicon and aluminum thermocouples with silicon nitride for absorption and passivation. Standard MEMS steps such as thermal oxidation, LPCVD, plasma-enhanced CVD (PECVD), and deep reactive ion etching (DRIE) were used. Circular and double-ended rectangular layouts were studied; the circular design offers higher responsivity and stability, while the rectangular structure provides a broader field of view but suffers from fragility because of the added adiabatic grooves. Aydin *et al.*[39] presented a MEMS-based uncooled IR sensor that utilizes a microbolometer structure encapsulated in wafer-level vacuum packaging. The sensor included a silicon-based cap with moth-eye grating structures on both sides to boost long-wave IR transmission to more than 80%. Fabrication involves DRIE, Au–In transient liquid phase bonding, and high-temperature glass frit bonding. Despite the advanced packaging, drawbacks include potential complexity in maintaining hermetic seals and challenges in getter integration for ultralow pressure, especially if high thermal budgets affect device performance.

CMOS-MEMS technology involves developing MEMS devices using a standard CMOS process, allowing mechanical structures to be fabricated directly within or alongside integrated circuits.[40–43] This approach enables the seamless integration of sensing or actuating components with on-chip signal processing, leading to significant advantages in system miniaturization and performance. The benefit is the reduced fabrication cost, as it leverages the existing CMOS infrastructure without the need for specialized MEMS foundries. This makes CMOS-MEMS highly suitable for applications requiring compact, low-cost, and high-performance sensors and microdevices.[44–47] In this study, we employ CMOS-MEMS technology to fabricate an IR sensor. The sensor is designed with a ring-shaped aluminum grating absorber to enhance thermal energy absorption at the hot end, thereby improving the sensor's voltage responsivity. Compared with the IR sensors developed by Bao *et al.*,[31] Lee *et al.*,[32] Tsai *et al.*,[33] Padha *et al.*,[34] Ho *et al.*,[35] Ahmadzadeh *et al.*,[36] Adiyan *et al.*,[37] Lei *et al.*,[38] and Aydin *et al.*,[39] the fabrication process in this study is simpler and more suitable for large-scale production using semiconductor foundries.

2. Design of the IR Sensor

Figure 1 shows the three-dimensional structure of the thermoelectric IR sensor composed of 32 thermopiles and a centrally located ring-shaped aluminum grating absorber. The hot junctions of the thermopiles and the absorber are positioned at the center of the sensor and designed as suspended structures to enhance thermal isolation from the silicon substrate. In contrast, the cold junctions of the thermopiles remain anchored to the silicon substrate, allowing a temperature gradient to form when the sensor is exposed to IR radiation. Figure 2 illustrates the thermopile architecture, highlighting the alternating arrangement of thermoelectric materials and the connection between the hot and cold junctions. The absorber plays a crucial role in the sensor's operation, as it captures incoming IR radiation and converts it into thermal energy, which then heats the hot junctions of the thermopiles. The ring-shaped grating design of the aluminum absorber enhances IR absorption efficiency by increasing the surface area and optimizing the interaction with incident IR waves. This efficient absorption is essential for generating a sufficient temperature difference across the thermopiles, thereby maximizing the sensor's voltage output and improving its overall sensitivity.

The output voltage of a thermoelectric IR sensor is determined by the Seebeck effect, which generates a voltage in response to a temperature difference across two dissimilar materials. The voltage output of the thermopile-based IR sensor can be expressed as[36]

$$V_{out} = N_u \left(\alpha_1 - \alpha_2\right)\Delta T\,, \tag{1}$$

where N_u is the number of thermopile pairs, α_1 and α_2 are the Seebeck coefficients of P-polysilicon and N-polysilicon, and ΔT is the temperature difference between the hot and cold junctions. To enhance the output voltage, several strategies can be applied on the basis of this relationship. First, increasing the number of thermopiles raises the total output voltage linearly,

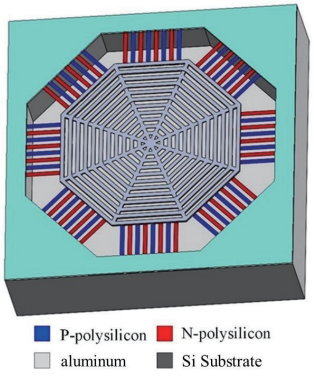

Fig. 1. (Color online) Three-dimensional structure of the IR sensor.

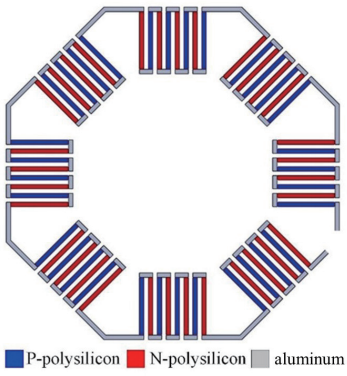

Fig. 2. (Color online) Thermopile architecture of the IR sensor.

as each additional junction contributes to the overall signal. Second, selecting material pairs with a larger Seebeck coefficient difference, such as combining polysilicon and aluminum, can significantly improve voltage generation efficiency. Third, maximizing the temperature difference ΔT between the hot and cold junctions is critical; this can be achieved by improving thermal isolation through suspended structures and by enhancing infrared absorption using specially designed absorbers such as ring-shaped gratings or multilayer aluminum films. These approaches reduce thermal conduction to the substrate while increasing the energy absorbed at the hot junction.

The voltage responsivity of a thermoelectric IR sensor is a critical parameter that defines how efficiently the sensor converts the absorbed infrared radiation into an electrical voltage. It is expressed as[31]

$$R_v = \frac{V_{out}}{P_{in}}, \tag{2}$$

where V_{out} is the output voltage generated by the sensor and P_{in} is the incident infrared power absorbed by the sensing area. This parameter essentially measures the sensitivity of the IR sensor; a higher voltage responsivity means that the sensor can detect weaker IR signals and produce a higher voltage output, which is essential for high-performance applications such as thermal imaging, environmental monitoring, and motion detection. Several factors directly affect the voltage responsivity. First, increasing the Seebeck coefficient difference between the two thermoelectric materials enhances the voltage output, thereby improving R_v. Second, incorporating effective absorber designs, such as ring-shaped aluminum gratings or multilayer metal films, increases the amount of IR radiation absorbed, increasing P_{in}. Third, the strong thermal isolation achieved through the adoption of suspended microstructures and etched cavities beneath the hot junction reduces heat loss to the substrate, thereby increasing the temperature gradient ΔT and enhancing V_{out}. In essence, the voltage responsivity encapsulates the overall efficiency of an IR sensor's design and materials in converting thermal energy into usable electrical signals.

The incident infrared power absorbed by the sensor can be estimated using the Stefan–Boltzmann law:[31,48,49]

$$P_{in} = \frac{\sigma \varepsilon A_s A_d C_p \left(T_s^4 - T_a^4\right)}{\pi d^2}, \tag{3}$$

where σ is the Stefan–Boltzmann constant, ε represents the emissivity of the blackbody source, A_s denotes the absorption area of the sensor, A_d is the radiation area of the IR source, and d is the distance between the sensor surface and the IR radiator, C_p is the root mean square conversion factor related to the chopper, T_s is the temperature of the IR source, and T_a is the ambient temperature. When all parameters in Eq. (3) are known or measured, the incident IR power absorbed by the sensor can be estimated using this formula.

3. Fabrication of the IR Sensor

An IR sensor was fabricated using the standard 0.35 μm CMOS process of Taiwan Semiconductor Manufacturing Company (TSMC). This sensor is composed of thermopiles and a ring-shaped grating absorber, both of which are suspended structures. The hot junctions of the thermopiles, along with the absorber, are suspended above the substrate to improve thermal isolation. The sensor's design layout was created with Cadence software, ensuring it fulfilled both mechanical and operational specifications. Fabrication was carried out by TSMC, which implemented the entire layout onto a silicon substrate through its standard CMOS process, enabling the accurate construction of all sensor elements.

Following the completion of the CMOS fabrication, a post-CMOS process was performed to further refine the sensor structure. This involved etching beneath the absorber and thermopile hot junctions to form cavities, which are crucial for minimizing heat loss and thereby enhancing the sensor's voltage responsivity and overall performance. The IR sensor's fabrication procedure is depicted in Fig. 3. As seen in Fig. 3(a), the cross section after the initial CMOS processing stage is presented. To create cavities beneath the thermopile hot junctions and absorber, a two-step post-processing sequence was employed. First, as illustrated in Fig. 3(b), reactive ion etching (RIE) with a CF_4/O_2 gas blend was used to eliminate the silicon dioxide layer, revealing the silicon beneath. Then, Fig. 3(c) shows the subsequent step, in which the silicon substrate itself was etched by SF_6/O_2-based RIE to form the necessary cavity structure beneath the suspended architecture. The absorber layer is made of stacked aluminum films, and the metal used throughout the design is aluminum, which is compatible with standard CMOS processes.

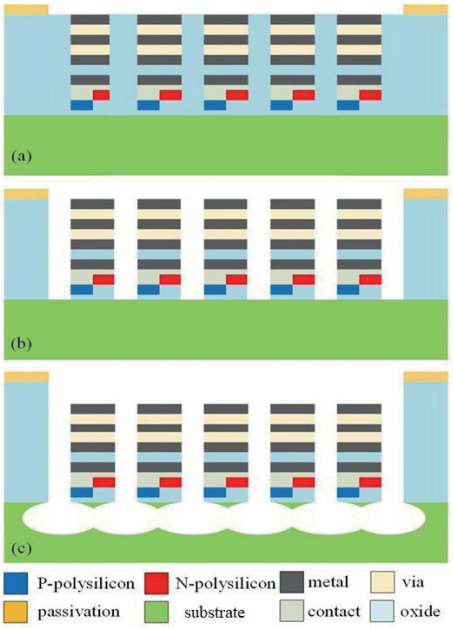

Fig. 3. (Color online) Process flow of the IR sensor: (a) after CMOS process; (b) etching silicon dioxide; (c) etching silicon subtrate.

The completed IR sensor was examined by both SEM[50] and optical microscopy (OM) to confirm the success of the fabrication steps. Figure 4 presents an optical microscope image of the IR sensor, clearly showing the centrally located ring-shaped aluminum grating absorber, which appears white in the image. The thermopile structures are also visibly defined around the absorber. Figure 5 provides a cross-sectional SEM image of the IR sensor, where the cavities and suspended structures are distinctly visible. This confirms that the post-CMOS etching process successfully removed the silicon substrate beneath the absorber and hot end of the thermopiles, effectively creating the necessary suspended architecture for improved thermal isolation.

Once the IR sensor chip was fully fabricated, wire bonding was performed to enable performance testing. This process connects the sensor's bonding pads to a printed circuit board (PCB) using fine gold wires. Figure 6 shows the OM image of the IR sensor after wire bonding, with visible gold wires linking the sensor to the PCB. These connections are essential for transmitting the sensor's output signals and conducting electrical measurements during functional testing. Overall, this fabrication approach demonstrates the successful implementation of CMOS-MEMS technology for IR sensor development, utilizing a foundry-compatible process and straightforward post-processing steps to achieve a high-performance, thermally isolated sensor structure suitable for large-scale production.

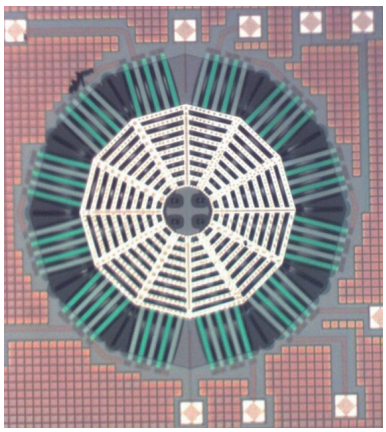

Fig. 4. (Color online) Optical image of the IR sensor.

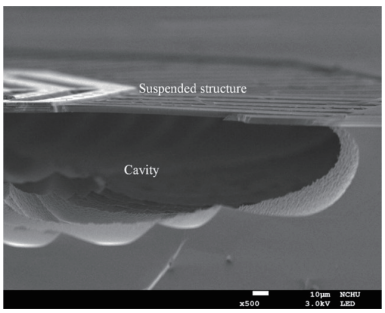

Fig. 5. (Color online) SEM image of the IR sensor.

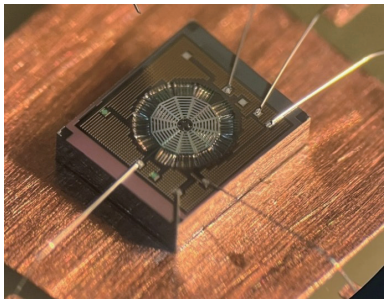

Fig. 6. (Color online) IR sensor connected to the PCB through wire bonding.

4. Results

The measurement setup for the IR sensor was established to assess its electrical response to IR radiation under controlled conditions. As illustrated in Fig. 7, the setup consists of a temperature-controlled blackbody radiator, a chopper, a digital multimeter, and an oscilloscope. The blackbody radiator serves as a stable and consistent IR radiation source directed toward the sensor. The chopper modulates the IR signal, allowing dynamic measurements to extract the sensor signal by locking onto the chopping frequency. The digital multimeter is used to monitor and record the sensor's voltage output. During testing, the IR sensor is wire-bonded to a PCB and connected to all relevant instruments. Once the IR source is turned on, IR radiation is focused onto the sensor. The chopper modulates the incoming radiation, and the resulting voltage output is amplified, measured, and recorded. Through this setup, the sensor's performance parameters, such as output voltage, response time, and voltage responsivity to various IR intensities or modulation frequencies, can be accurately characterized.

To measure its output voltage, the IR sensor was exposed to a known and controllable infrared radiation source, specifically a blackbody. During the experiment, the temperature of the blackbody radiator was gradually increased to vary the emitted IR power, while the corresponding output voltage of the IR sensor was recorded using a digital multimeter. Figure 8 shows the measured output voltage of the IR sensor as a function of the blackbody temperature. As illustrated in Fig. 8, the sensor produced an output voltage of 18.9 mV at 313 K, which increased to 31.1 mV when the temperature rose to 373 K.

The amount of incident power received by the sensor was estimated using the Stefan–Boltzmann law, taking into account the radiator's temperature, emission area, and the distance between the radiator and the sensor. In this experiment, the parameters were set as follows: ε = 0.98, A_s = 2 mm^2, A_d = 78.5 cm^2, d = 25 cm, and T_a = 298 K. By substituting these values along with the data presented in Fig. 8 into Eq. (3), the relationship between the output voltage and the incident infrared power was determined. The graph in Fig. 9 illustrates this correlation, where the slope of the linear region represents the voltage responsivity defined by Eq. (2)—the ratio of

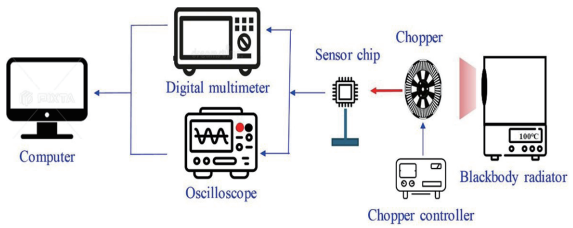

Fig. 7. (Color online) Measurement setup for the IR sensor.

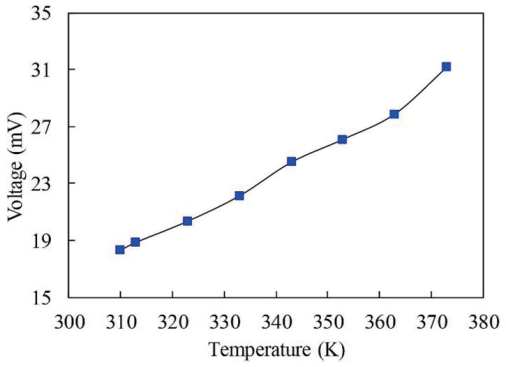

Fig. 8. (Color online) Measured output voltage of the IR sensor.

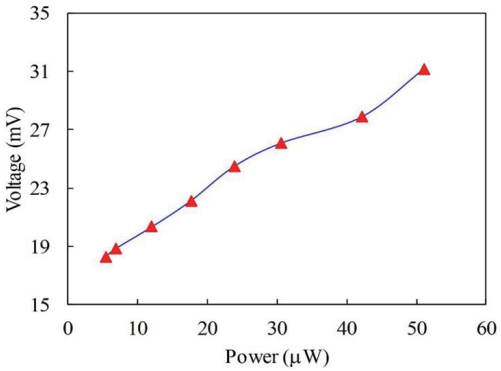

Fig. 9. (Color online) Relationship between the output voltage and the incident power for the IR sensor.

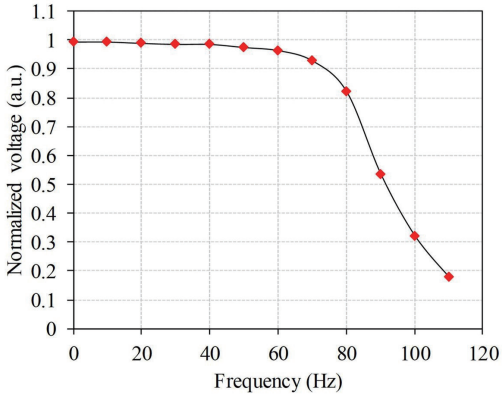

Fig. 10. (Color online) Relationship between the normalized output voltage and the modulation frequency.

the change in output voltage to the change in incident power. From this linear fit, the voltage responsivity of the IR sensor was determined to be 276 V/W, indicating its effectiveness in converting infrared radiation into electrical signals.

To evaluate the response time of the IR sensor, a modulated IR signal was used to assess how rapidly the sensor responds to variations in incident radiation. As illustrated in Fig. 7, a blackbody radiator maintained at 363 K provides a stable IR radiation source, while an optical chopper periodically blocks and transmits the radiation, producing a square wave signal with a controlled frequency. By adjusting the chopping frequency and measuring the sensor's output voltage (root mean square value), the dynamic response characteristics of the sensor can be investigated. As the chopping frequency increases, the sensor output begins to decline, indicating a limitation in its ability to follow rapidly changing signals. Figure 10 presents the relationship between the normalized output voltage and the modulation frequency. The response time is determined on the basis of the cutoff frequency ($f_{cut\text{-}off}$), defined as the frequency at which the output voltage drops to 70.7% of its maximum at low frequencies. The response time τ is calculated as $\tau = 1/(2\pi f_{cut\text{-}off})$.[51] According to Fig. 10, the IR sensor exhibits a cutoff frequency of 84.2 Hz, corresponding to a response time of approximately 2.2 ms.

5. Conclusions

In this work, we demonstrated the successful design, fabrication, and characterization of a CMOS-based thermoelectric IR sensor featuring a suspended ring-shaped aluminum grating absorber and 32 thermopile junctions. By utilizing the standard 0.35 μm CMOS process of TSMC and a simplified two-step post-CMOS etching technique, the proposed IR sensor achieved both structural precision and functional efficiency while maintaining compatibility with large-scale semiconductor manufacturing. The suspended architecture of the absorber and thermopile hot junctions significantly improved thermal isolation from the silicon substrate,

enhancing the temperature gradient and resulting in a stronger voltage response owing to the Seebeck effect. Performance evaluations confirmed the sensor's high sensitivity and fast dynamic behavior. The voltage responsivity reached 276 V/W, as extracted from the linear relationship between the output voltage and the incident infrared power. In addition, the response time was measured to be approximately 2.2 ms. These results indicate that the sensor can accurately and rapidly respond to various IR stimuli, making it well suited for applications such as motion detection, noncontact temperature sensing, and thermal imaging. The integration of a ring-shaped aluminum grating absorber not only improves infrared absorption efficiency but also represents a novel approach to enhancing sensor performance without significantly increasing design complexity.

Acknowledgments

The authors would like to thank the National Science and Technology Council of R.O.C. for financial support under the Grant NSTC-113-2221-E-005-061. The authors also gratefully acknowledge the technical support provided by Mu-Chien Wang and Chun-Yu Wu from the MEMS Lab at National Chung Hsing University and the Taiwan Semiconductor Research Institute (TSRI), NIAR.

References

1 A. Mohammad, Modabbir, I. Ashraf, and M. M. Kamal: J. Instit. Eng. (India): Series B **104** (2023) 679. https://doi.org/10.1007/s40031-023-00885-0
2 A. Rogalski: Prog. Quantum Electron. **27** (2003) 59. https://doi.org/10.1016/S0079-6727(02)00024-1
3 J. Peltola, T. Hieta, and M. Vainio: Opt. Lett. **40** (2015) 2933. https://doi.org/10.1364/OL.40.002933
4 Y. Zhao and J. H. M. Bergmann: Sensors **23** (2023) 7439. https://doi.org/10.3390/s23177439
5 Z. Wen, L. Xie, H. Feng, and Y. Tan: Neurocomputing **337** (2019) 67. https://doi.org/10.1016/j.neucom.2019.01.045
6 M.-Z. Poh, D. J. McDuff, and R. W. Picard: Opt. Express **18** (2010) 10762. https://doi.org/10.1364/OE.18.010762
7 Z. Zhou, Y. Majeed, G. Diverres Naranjo, and E. M. T. Gambacorta: Comput. Electron. Agri. **182** (2021) 106019. https://doi.org/10.1016/j.compag.2021.106019
8 R. A. Osornio-Rios, J. A. Antonino-Daviu, and R. D. J. Romero-Troncoso: IEEE Trans. Ind. Inf. **15** (2019) 615. https://doi.org/10.1109/TII.2018.2884738
9 R. E. Nogales and M. E. Benalcázar: Int. J. Mach. Learn. Cybern. **12** (2021) 2859. https://doi.org/10.1007/s13042-021-01372-y
10 M. Carosena and M. C. Giovanni: Meas. Sci. Technol. **15** (2004) R27. https://doi.org/10.1088/0957-0233/15/9/R01
11 G.-J. Guo and J.-M. Jehng: Sens. Mater. **36** (2024) 363. https://doi.org/10.18494/SAM4776
12 Y.-X. Shen, Y.-C. Tsai, C.-Y. Lee, C.-C. Wu, and C.-L. Dai: Micromachines **13** (2022) 1258. https://doi.org/10.3390/mi13081258
13 D. Yamane, K. Kawashima, R. Sugimoto, R. Li, H. Kayaguchi, K. Kurihara, H. Ishii, and Y. Tanaka: Sens. Mater. **35** (2023) 1985. https://doi.org/10.18494/SAM4400
14 C.-L. Dai, H.-L. Chen, and P.-Z. Chang: J. Micromech. Microeng. **11** (2001) 612. https://doi.org/10.1088/0960-1317/11/5/326
15 Z.-X. Dai and C.-Y. Chen: Energy Convers. Manag. X **24** (2024) 100748. https://doi.org/10.1016/j.ecmx.2024.100748
16 D. Ching-Liang, X. Fu-Yuan, J. Ying-Zong, and C. Chin-Fon: J. Micromech. Microeng. **15** (2005) 98. https://doi.org/10.1088/0960-1317/15/1/015
17 T.-Y. Lai, G.-C. Chen, and Y. Hsiao: Sens. Mater. **35** (2023) 1141. https://doi.org/10.18494/SAM4239
18 J.-Z. Tseng, C.-C. Wu, and C.-L. Dai: Sensors **14** (2014) 6722. https://doi.org/10.3390/s140406722

19 Y.-H. Yen, C.-S. Hsu, Z.-Y. Lei, H.-J. Wang, C.-Y. Su, C.-L. Dai, and Y.-C. Tsai: Micromachines **13** (2022) 1220. https://doi.org/10.3390/mi13081220
20 C.-Y. Lee, Z.-Y. Huang, J.-Y. Hsu, T.-F. Kuo, and Z.-X. Dai: Sens. Mater. **37** (2025). https://doi.org/10.18494/SAM5139
21 H.-J. Wang, T.-Y. Cheng, C.-C. Huang, C.-Y. Su, C.-L. Dai, and Y.-C. Tsai: Jap. J. Appl. Phys. **60** (2021) SCCD04. https://doi.org/10.35848/1347-4065/abe2e6
22 C.-L. Dai: Sens. Actuators, B **122** (2007) 375. https://doi.org/10.1016/j.snb.2006.05.042
23 J. Mizuno: Sens. Mater **35** (2023). https://doi.org/10.18494/SAM4411
24 C.-L. Dai, H.-M. Hsu, M.-C. Tsai, M.-M. Hsieh, and M.-W. Chang: Microelectronics J. **38** (2007) 519. http://dx.doi.org/10.1016/j.mejo.2007.03.012
25 C.-L. Dai and Y.-L. Chen: Sensors **7** (2007) 2660. https://doi.org/10.3390/s7112670
26 C.-L. Dai, H.-J. Peng, M.-C. Liu, C.-C. Wu, H.-M. Hsu, and L.-J. Yang: Jap. J. Appl. Phys. **44** (2005) 6804. https://doi.org/10.1143/JJAP.44.6804
27 Z. Xiong, C.-Y. Tsai, and C.-Y. Lee: Sens. Mater. **36** (2024). https://doi.org/10.18494/SAM5124
28 D. Xu, Y. Wang, B. Xiong, and T. Li: Front. Mech. Eng. **12** (2017) 557. https://doi.org/10.1007/s11465-017-0441-2
29 T. Saraf, I. Brouk, S. B.-L. Shefi, A. Unikovsky, T. Blank, P. K. Radhakrishnan, and Y. Nemirovsky: IEEE J. Electron Devices Soc. **4** (2016) 155. https://doi.org/10.1109/JEDS.2016.2539980
30 S. P. Gaur, K. Rangra, and D. Kumar: Sens. Actuators, A **300** (2019) 111660. https://doi.org/10.1016/j.sna.2019.111660
31 A. Bao, C. Lei, H. Mao, R. Li, and Y. Guan: Micromachines **10** (2019) 877. https://doi.org/10.3390/mi10120877
32 C.-Y. Lee, C.-X. Yu, K.-Y. Lin, and L.-M. Fu: Appl. Sci. **11** (2021) 9074. https://doi.org/10.3390/app11199074
33 C.-Y. Tsai, Y.-W. Lin, H.-M. Ku, and C.-Y. Lee: Sensors **23** (2023) 6818. https://doi.org/10.3390/s23156818
34 B. Padha, I. Yadav, S. Dutta, and S. Arya: ACS Appl. Electron. Mater. **5** (2023) 5386. https://doi.org/10.1021/acsaelm.3c00860
35 J.-J. Ho, Y. K. Fang, W. J. Lee, F. Y. Chen, W. T. Hsieh, S. F. Ting, M. S. Ju, S. B. Huang, W. Kun-Hsien, and C. Y. Chen: IEEE Trans. Electron Devices **46** (1999) 2289. https://doi.org/10.1109/16.808059
36 S. Ahmadzadeh, D. Gibson, L. Fleming, D. Hutson, S. Song, A. James, S. Wells, A. Forsyth, and S. Bruckshaw: Appl. Opt. **62** (2023) B79. https://doi.org/10.1364/AO.477050
37 U. Adiyan, F. Civitci, O. Ferhanoglu, H. Torun, and H. Urey: IEEE Photonics Technol. Lett. **28** (2016) 1866. https://doi.org/10.1109/LPT.2016.2574123
38 C. Lei, Y. Guan, T. Liang, X. Wu, Y. Bai, M. Gong, P. Jia, and J. Xiong: Photonic Sens. **13** (2023) 230309. http://dx.doi.org/10.1007/s13320-023-0682-0
39 G. D. Aydin, O. S. Akar, and T. Akin: Micromachines **15** (2024) 935. https://doi.org/10.3390/mi15080935
40 C. H. Wu, P. J. Shih, Y. C. Tsai, and C. L. Dai: Sensors **21** (2021) 6953. https://doi.org/10.3390/s21216953
41 Z. X. Dai, R. W. Tsai, and Q. H. Shih: IEEE Sens. J. **25** (2025) 9540. https://doi.org/10.1109/JSEN.2025.3537107
42 M.-Z. Yang, C.-L. Dai, P.-J. Shih, and Z.-Y. Tsai: Microelectron. Eng. **88** (2011) 2242. https://doi.org/10.1016/j.mee.2010.12.115
43 Z.-X. Dai, C.-Y. Chen, B.-C. Chiu, and C.-Y. Lee: J. Micromech. Microeng. **34** (2024) 075001. https://doi.org/10.1088/1361-6439/ad520b
44 C.-L. Dai and M.-C. Liu: Jap. J. Appl. Phys. **46** (2007) 843. https://doi.org/10.1143/JJAP.46.843
45 Z. X. Dai and M. H. You: IEEE Sensors J. **24** (2024) 34217. https://doi.org/10.1109/JSEN.2024.3452109
46 M. Z. Yang, C. L. Dai, and C. C. Wu: Sensors **14** (2014) 20360. https://doi.org/10.3390/s141120360
47 Z.-X. Dai, W.-H. Li, and Y.-N. Liu: J. Micromech. Microeng. **35** (2025) 065005. https://doi.org/10.1088/1361-6439/addb55
48 H. Zhou, P. Kropelnicki, J. M. Tsai, and C. Lee: J. Micromech. Microeng. **23** (2013) 065026. https://doi.org/10.1088/0960-1317/23/6/065026
49 S. J. Chen and B. Chen: Sensors **20** (2020) 4007. https://doi.org/10.3390/s20144007
50 T.-Y. Chiang and C.-L. Dai: Nanoscale Res. Lett. **7** (2012) 263. https://doi.org/10.1186/1556-276X-7-263
51 P. S. Lin, T. W. Shen, K. C. Chan, and W. Fang: IEEE Sens. J. **20** (2020) 11105. https://doi.org/10.1109/JSEN.2020.2997534